ELSEVIER

Journal of Fluids and Structures 20 (2005) 51–69

JOURNAL OF FLUIDS AND STRUCTURES

www.elsevier.com/locate/jfs

Computation of dynamic fluid–structure interaction in two-dimensional laminar flows using combined formulation

K. Namkoong[a], H.G. Choi[b], J.Y. Yoo[a,*]

[a]*School of Mechanical and Aerospace Engineering, Seoul National University, San 56-1, Shinlim-dong, Kwanak-gu, Seoul 151-742, Republic of Korea*

[b]*Department of Mechanical Engineering, Seoul National University of Technology, 172, Gongreung-2-dong, Nowon-gu, Seoul 139-743, Republic of Korea*

Received 30 September 2002; accepted 14 June 2004
Available online 31 December 2004

Abstract

In fluid-structure interaction (FSI) problems, two different governing equations are solved together. In addition, a kinematic constraint should be imposed along the boundary between the fluid and the structure. We use the combined formulation which incorporates both the fluid and structure equations of motion into a single coupled variational equation. This does not necessitate the calculation of the fluid force on the surface of the structure explicitly when solving the equation of motion for the structure. A two-dimensional laminar channel flow divided by a plate and another two-dimensional laminar flow caused by the oscillation of a vertical plate in a cavity filled with a fluid are considered to investigate the dynamic FSI between the fluid and the plate. The Navier–Stokes equation modified with the arbitrary Lagrangian–Eulerian (ALE) technique is solved using a P2P1 Galerkin finite element method (FEM). The equation of motion for the plate is solved using a Galerkin FEM without considering the internal structural damping effect. Numerical results for steady channel flow are in good agreement with the existing work of Wang. In addition to the Reynolds number, two nondimensional parameters, which govern this fluid–structure system, are proposed. When the Reynolds number and the geometry are fixed, it is noted that the damping of the amplitude of plate oscillation increases as the dynamic viscosity and the density of the fluid increase, and that the added mass is linearly proportional to the fluid density but independent of fluid viscosity.

1. Introduction

A variety of physical phenomena caused by fluid–structure interaction (FSI) can be encountered in many engineering applications, such as the stability and response of aircraft wings, the pulsating blood flow through arteries, the response of bridges and tall buildings to wind and the vibration of turbine and compressor blades, and the oscillation of heat exchangers (Dowell and Hall, 2001).

In the FSI problems, two different governing equations are solved together. One is for the fluid and the other for the structure. Furthermore, a kinematic constraint should be imposed along the boundary between the fluid and the structure. Recent progress in computing power has led to a great advance in computational fluid dynamics (CFD) and

*Corresponding author. Tel.: +82 2 880 7112; fax: +82 2 883 0179.
E-mail address: jyyoo@snu.ac.kr (J.Y. Yoo).

0889-9746/$ - see front matter © 2004 Elsevier Ltd. All rights reserved.
doi:10.1016/j.jfluidstructs.2004.06.008

computational structural dynamics (CSD), so that many researchers are trying to solve the FSI problems by coupling the equation of motion for the fluid with that for the structure. Nevertheless, to treat the equation of motion for the fluid in complex FSI problems, most researchers have adopted the Laplace (potential flow) equation (Ergin and Uğurlu, 2003; Lam et al., 2002) or the Euler equation, because they still require substantial computing power without simplification or modeling. In fact, in some simulations, oversimplifications on the structure side (Frandsen, 1999) or the fluid side (Kovacs, 1994; Zahlten, 1998) have been made for the FSI simulation, not only because the full simulation of both the fluid and structure is very complex, but also because the computing power has not been sufficient. More recently, some research groups (Glück et al., 2003; Slone et al., 2002; Zhang et al., 2003) have tried to solve the full coupling between the fluid flow and the motion of the structure without resort to assumptions made by previous researchers. According to Zhang et al. (2003), the fully coupled simulation methods can be grouped into two categories. In a ''direct computing method'', fluid variables are determined together with the variables of the structural system simultaneously. Thus, a global matrix that includes both the fluid variables (velocity and pressure) and the structural variables (displacement) has to be solved at the same time. Compatibility conditions and a mapping process (Zhang et al., 2003) need not be considered, because a combined global matrix including both the fluid and the structural variables is solved simultaneously. On the other hand, we note that the time and effort to develop a directly coupled FSI code from scratch are the price we have to pay for the sake of robustness and efficiency of that code. In an ''iterative computing method'', two separate global matrices, one for the fluid and the other for the structure, have to be solved sequentially. Some additional constraints such as traction equilibrium and displacement compatibility between the fluid and structure domains must be imposed by sub-iterations (Glück et al., 2003; Slone et al., 2002; Zhang et al., 2003). Therefore, an iterative computing method might require more CPU time than a direct computing method due to the sub-iteration which is repeatedly performed until the whole (fluid plus structure) system has converged. On the other hand, an iterative computing method has an advantage over a direct computing method in the sense that the modularity of each of the fluid and structure codes can be maintained. Thus, integration of well-established fluid and structure codes into a single FSI code is quite possible. It is also noted in passing that a few works using reduced order models (ROMs) such as proper orthogonal decomposition (POD) have been reported recently (Dowell and Hall, 2001).

Hesla (1991) earlier proposed the *combined formulation* that incorporates both the equation of motion for the fluid and that for the structure into a single coupled variational equation. With this formulation, it is not necessary to calculate the fluid force on the surface of the structure explicitly when solving the equation of motion for the structure. In other words, fluid traction on the surface of a structure is not a function of known fluid velocity and pressure fields, but a function of unknown fluid velocity and pressure fields which are to be determined together with the variables of the structure system simultaneously.

Hu (1996) implemented successfully this combined formulation for the first time in the direct numerical simulation (DNS) of sedimentation of 100 or 400 particles in a vertical channel due to gravity and a pressure gradient in the opposite direction to gravity, by adopting the Navier–Stokes equation for the fluid side in conjunction with the explicit-implicit scheme of Hu et al. (1992) and the arbitrary Lagrangian–Eulerian (ALE) technique where the mesh velocities are also dealt with implicitly and computed iteratively. He found that particles are away from the wall and there exists a lubrication layer near the wall when the pressure gradient is sufficiently larger than the gravity force, and that particles interact strongly and clusters of particles appear as the particle Reynolds number becomes larger. Later, Choi (2000) proposed a splitting method for the DNS of the fluid–particle problem using the combined formulation, a fractional four-step method, and the ALE technique, where a symmetric pressure equation was adopted. Choi and Joseph (2001) performed a DNS of fluidization by lift of 300 circular particles in plane Poiseuille flow using the combined formulation and the ALE technique. Hu et al. (2001) summarized the methods for numerical simulation of fluid–solid systems and presented the most up-to-date implementation method for DNS using the combined formulation, the explicit–implicit scheme, and the ALE technique.

The objective of the present study is to develop a combined formulation that can be used for solving the dynamic FSI problem. We first investigate the dynamic FSI in a two-dimensional laminar channel flow divided by a plate, because some analytical solutions of the static counterpart of this problem are available (Wang, 1999), which can serve for validating the numerical code developed in the present study. Although he investigated both laminar and turbulent flows, he only considered steady cases, not dynamic FSI problems. However, this problem is associated with a well-defined geometry and can serve as a basis for more complex FSI problems. The dividing plate can be considered as a beam, so that we use the Bernoulli–Euler beam model, which is the simplest structural form that can support a bending moment. Next, we consider another dynamic FSI problem, i.e. oscillation of a vertical plate in a cavity filled with a fluid, because the results of a three-dimensional coupled simulation for the same FSI problem is also available (Glück et al., 2001). Although they performed three-dimensional simulations, both the fluid and the plate showed two-dimensional behavior, because of the symmetric boundary conditions in the spanwise direction. Since the key idea of the present combined formulation is to treat the traction on the structure due to fluid motion implicitly, the complexity

of the combined formulation does not increase, even though the governing equation for the structure becomes more complicated. More details of the coupling (combined) procedure of the present combined formulation, will be given in Section 2, where it is discussed that this implicit method is stabler than the explicit method. In addition to the Reynolds number, two nondimensional parameters, which govern the FSI problem, are suggested in Section 3. Validation of the code developed in the present study is made in Section 4.1. The dynamic FSIs are investigated in Sections 4.2 and 4.3, where the damping of the plate oscillation and the effect of the added mass on the frequency response of the plate are discussed. Conclusions are drawn in Section 5.

2. Numerical methods

A P2P1 Galerkin FEM is applied to the Navier–Stokes equation incorporating the ALE technique, and a Galerkin FEM is applied to the equation of motion for the beam. Then, these two equations are consolidated and solved using the combined formulation and a modified explicit–implicit scheme.

2.1. Governing equations for the FLUID

The governing equations for the incompressible fluid flow are the Navier–Stokes equation and the continuity equation. In FSI problems, the interface between the fluid and the structure may change in time and the computational domain should be changed accordingly. To accomplish this, we adopt the ALE technique, where the mesh velocity $\mathbf{u}_m$ is computed by solving the Laplace equation with appropriate boundary conditions. Applying a P2P1 Galerkin finite element method to the Navier–Stokes equation in conjunction with the ALE technique and to the continuity equation, and invoking the divergence theorem, the problem to be solved and the equations involved are as follows.

Find $\mathbf{u} \in H_h^1(\Omega)$, $p \in L_h^2(\Omega)$ such that

$$\int_\Omega \left[\mathbf{W}\cdot\rho_f\left(\frac{\partial \mathbf{u}}{\partial t}+\{(\mathbf{u}-\mathbf{u}_m)\cdot\nabla\}\mathbf{u}\right)+\nabla\mathbf{W}:\tilde{\sigma}\right]\mathrm{d}\Omega-\oint_\Gamma \mathbf{W}\cdot(\tilde{\sigma}\cdot\mathbf{n})\,\mathrm{d}\Gamma+\int_\Omega q(\nabla\cdot\mathbf{u})\,\mathrm{d}\Omega=0 \tag{1a}$$

for all admissible functions $\mathbf{W}=V_h$, $q\in P_h$, where

$$V_h=\{\mathbf{W}|\mathbf{W}\in H_h^1(\Omega),\ \mathbf{W}=\mathbf{0}\ \text{on}\ \Gamma_g\},\ P_h=\{q|q\in L_h^2(\Omega)\},$$
$$\tilde{\sigma}=-p\tilde{I}+\tilde{\tau},\ \tilde{\tau}=\mu[\nabla\mathbf{u}+(\nabla\mathbf{u})^{\mathrm{T}}]. \tag{1b}$$

In the above equation, $\mathbf{u}$ is the fluid velocity, p is the pressure, Ω is the fluid domain, $\mathbf{W}$ is the weighting function vector for the momentum equation [each component of W is a second-order polynomial such that $\mathbf{W}=\sum_i(\alpha_i F_i\mathbf{e}_x+\beta_i F_i\mathbf{e}_y+\gamma_i F_i\mathbf{e}_z)$, where α_i, β_i, and γ_i are arbitrary constants, F_i (the shape function for the velocity at the ith node point) is a second-order polynomial, and e_x, e_y, and e_z are the unit vectors in the x-, y-, and z-directions, respectively], ρ_f is the fluid density, t is the time, $\tilde{\sigma}$ is the stress tensor, Γ is the boundary of Ω, $\mathbf{n}$ is the outward unit normal vector to Γ, q is the weighting function for the continuity equation [$q=\sum_i\lambda_i G_i$, λ_i is an arbitrary constant and G_i (the shape function for the pressure at the ith node point) is a first-order polynomial], Γ_g is a part of Γ on which the Dirichlet boundary condition is imposed, $\tilde{I}$ is the second-order identity tensor, $\tilde{\tau}$ is the shear stress tensor, μ is the dynamic viscosity of the fluid. The Crank–Nicolson scheme, which is second-order accurate and unconditionally stable, is used for time integration. Assembling element matrices obtained through the above procedure, the following equation for the global matrix is obtained:

$$\begin{bmatrix} A_{ij}^{uu} & A_{ij}^{uv} & B_{ij}^{u} \\ A_{ij}^{vu} & A_{ij}^{vv} & B_{ij}^{v} \\ (B_{ij}^{u})^{\mathrm{T}} & (B_{ij}^{v})^{\mathrm{T}} & 0 \end{bmatrix}\begin{pmatrix} u_j^{n+1} \\ v_j^{n+1} \\ p_j^{n+1} \end{pmatrix}=\begin{pmatrix} f_i^u \\ f_i^v \\ 0 \end{pmatrix}, \tag{2}$$

where

$$A_{ij}^{uu}=\int_\Omega\left[\frac{F_iF_j}{\Delta t}+\frac{1}{2}F_i\left(F_k\{u_k^{n+1}-(u_m)_k^{n+1}\}\frac{\partial F_j}{\partial x}+F_k\{v_k^{n+1}-(v_m)_k^{n+1}\}\frac{\partial F_j}{\partial y}\right)+\frac{1}{2}\nu_f\left(2\frac{\partial F_i}{\partial x}\frac{\partial F_j}{\partial x}+\frac{\partial F_i}{\partial y}\frac{\partial F_j}{\partial y}\right)\right]\mathrm{d}\Omega,$$
$$A_{ij}^{uv}=\int_\Omega\left[\frac{1}{2}\nu_f\frac{\partial F_i}{\partial y}\frac{\partial F_j}{\partial x}\right]\mathrm{d}\Omega,\ A_{ij}^{vu}=\int_\Omega\left[\frac{1}{2}\nu_f\frac{\partial F_i}{\partial x}\frac{\partial F_j}{\partial y}\right]\mathrm{d}\Omega,$$

$$A_{ij}^{vv} = \int_{\Omega} \left[\frac{F_i F_j}{\Delta t} + \frac{1}{2} F_i \left(F_k \{u_k^{n+1} - (u_m)_k^{n+1}\} \frac{\partial F_j}{\partial x} + F_k \{v_k^{n+1} - (v_m)_k^{n+1}\} \frac{\partial F_j}{\partial y} \right) + \frac{1}{2} v_f \left(\frac{\partial F_i}{\partial x}\frac{\partial F_j}{\partial x} + 2\frac{\partial F_i}{\partial y}\frac{\partial F_j}{\partial y} \right) \right] \mathrm{d}\Omega,$$

$$B_{ij}^{u} = \int_{\Omega} \left[-\frac{1}{\rho_f} \frac{\partial F_i}{\partial x} G_j \right] \mathrm{d}\Omega, \; B_{ij}^{v} = \int_{\Omega} \left[-\frac{1}{\rho_f} \frac{\partial F_i}{\partial y} G_j \right] \mathrm{d}\Omega,$$

$$(B_{ij}^{u})^{\mathrm{T}} = \int_{\Omega} \left[G_i \frac{\partial F_j}{\partial x} \right] \mathrm{d}\Omega, \; (B_{ij}^{v})^{\mathrm{T}} = \int_{\Omega} \left[G_i \frac{\partial F_j}{\partial y} \right] \mathrm{d}\Omega,$$

$$f_i^u = \int_{\Omega} \left[\frac{F_i F_k u_k^n}{\Delta t} - \frac{1}{2} F_i \left(F_k \{u_k^n - (u_m)_k^n\} \frac{\partial F_j}{\partial x} + F_k \{v_k^n - (v_m)_k^n\} \frac{\partial F_j}{\partial y} \right) u_j^n \right.$$
$$\left. - \frac{1}{2} v_f \left\{ \left(2\frac{\partial F_i}{\partial x}\frac{\partial F_j}{\partial x} + \frac{\partial F_i}{\partial y}\frac{\partial F_j}{\partial y} \right) u_j^n + \frac{\partial F_i}{\partial y}\frac{\partial F_j}{\partial x} v_j^n \right\} \right] \mathrm{d}\Omega,$$

$$f_i^v = \int_{\Omega} \left[\frac{F_i F_k v_k^n}{\Delta t} - \frac{1}{2} F_i \left(F_k \{u_k^n - (u_m)_k^n\} \frac{\partial F_j}{\partial x} + F_k \{v_k^n - (v_m)_k^n\} \frac{\partial F_j}{\partial y} \right) v_j^n \right.$$
$$\left. - \frac{1}{2} v_f \left\{ \frac{\partial F_i}{\partial x}\frac{\partial F_j}{\partial y} u_j^n + \left(\frac{\partial F_i}{\partial x}\frac{\partial F_j}{\partial x} + 2\frac{\partial F_i}{\partial y}\frac{\partial F_j}{\partial y} \right) v_j^n \right\} \right] \mathrm{d}\Omega.$$

In the above equations, (u, v) are the fluid velocity components in the Cartesian coordinates (x, y), (u_m, v_m) are the mesh velocity components, v_f is the kinematic viscosity of the fluid, the superscripts n, $n+1$ denote the nth and $(n+1)$th time steps, respectively, and the subscripts i, j, k denote the ith, jth, and kth nodes, respectively.

2.2. Governing equation for the beam

As previously mentioned and shown in Fig. 1, a two-dimensional plate can be considered as a beam, so that we use the Bernoulli–Euler beam model, which is the simplest structural form that can support the bending moment. A Bernoulli–Euler beam element is shown in Fig. 2, which is known to give accurate results when $h/\Delta L < 0.01$.

The governing equation describing the vibration of the Bernoulli–Euler beam is as follows:

$$\rho_s A \frac{\partial^2 w}{\partial t^2} + EI \frac{\partial^4 w}{\partial x^4} = f_s(x, t), \tag{3}$$

where ρ_s is the beam density, A is the beam cross-sectional area, w is the beam displacement, E is Young's modulus of elasticity, I is the second moment of the beam cross-sectional area, and $f_s(x, t)$ is the load per unit beam length. Applying the Galerkin FEM to Eq. (3), we obtain

$$\begin{gathered} [M]\ddot{\mathbf{d}} + [C]\dot{\mathbf{d}} + [K]\mathbf{d} = \mathbf{f}_p, \\ [M] = \int \rho_s \mathbf{N}^{\mathrm{T}} \mathbf{N} \, \mathrm{d}V, \; \mathbf{d}^{\mathrm{T}} = \begin{bmatrix} w_L, & \theta_L, & w_R, & \theta_R \end{bmatrix}, [K] = \int \mathbf{B}^{\mathrm{T}} D \mathbf{B} \, \mathrm{d}x, \\ \mathbf{N} = \begin{bmatrix} N_{w_L}, & N_{\theta_L}, & N_{w_R}, & N_{\theta_R} \end{bmatrix}, \quad \mathbf{B} = -\frac{\partial^2 \mathbf{N}}{\partial x^2}, \; D = EI = E\frac{bh^3}{12}, \\ \mathbf{f}_p = \int \mathbf{N}^{\mathrm{T}} f_s(x, t) \, \mathrm{d}x, \end{gathered} \tag{4}$$

where $[M]$ is the mass matrix, $\mathbf{d}$ is the displacement vector, (w_L, θ_L) and (w_R, θ_R) are the displacement and the deflection angle at the left and right nodes of the beam element, $[C]$ is the damping matrix, $[K]$ is the stiffness matrix, $\mathbf{N}$ is the shape matrix, $\mathbf{B}$ is the strain-displacement matrix, D is the stress–strain constant, $\mathbf{f}_p$ is the load vector, and b is the beam depth,

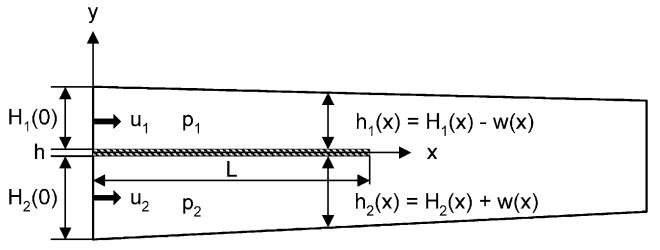

Fig. 1. Schematic diagram of a two-dimensional channel flow divided by a plate.

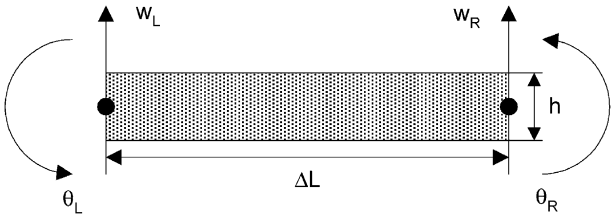

Fig. 2. A Bernoulli–Euler beam element.

which is unity in the present study. The damping matrix $[C] = [0]$ because the structural or internal damping is neglected in the present study. Applying the average acceleration method or the trapezoidal rule for time integration of Eq. (4), which is again second-order accurate and unconditionally stable, we obtain

$$\left(\frac{4}{(\Delta t)^2}[M] + [K]\right)\mathbf{d}^{n+1} + b\int \mathbf{N}^{\mathrm{T}}\left(G_L p_L^{n+1} + G_R p_R^{n+1}\right)\mathrm{d}x$$
$$= [M]\left(\frac{4}{(\Delta t)^2}\mathbf{d}^n + \frac{4}{\Delta t}\dot{\mathbf{d}}^n + \ddot{\mathbf{d}}^n\right) + [C]\left(\frac{2}{\Delta t}\mathbf{d}^n + \dot{\mathbf{d}}^n\right). \tag{5}$$

The second term on the left-hand side includes the fluid pressure on the beam at the next time step, which is combined with the beam displacement implicitly. Through this term, the fluid and the beam interact with each other, which is the main point of the combined formulation. The reason why this term appears on the left-hand side, not on the right-hand side, is that the governing equations for the fluid and the beam (structure) are to be solved simultaneously through the combined formulation, as will be explained in the next subsection.

2.3. The combined formulation and the explicit–implicit scheme

As previously mentioned, the combined formulation was proposed by Hesla (1991) and implemented first by Hu (1996) for practical application, which incorporates both the equation of motion for the fluid and that for the structure into a single coupled variational equation so that the fluid forces acting on the surface of the structure do not explicitly appear in the formulation. This is quite natural, since those fluid forces are internal when the fluid and the structure are considered as one single system (Hu et al., 2001). In the present combined formulation, the flow variables (u, v, p) and the beam variables (w, θ) are computed not separately but simultaneously by the total global matrix written in the form

$$\begin{bmatrix} A^{uu} & A^{uv} & B^u & 0 & 0 \\ A^{vu} & A^{vv} & B^v & C & 0 \\ (B^u)^{\mathrm{T}} & (B^v)^{\mathrm{T}} & 0 & 0 & 0 \\ 0 & 0 & D^w & E^{ww} & E^{w\theta} \\ 0 & 0 & D^\theta & E^{\theta w} & E^{\theta\theta} \end{bmatrix} \begin{bmatrix} u \\ v \\ p \\ w \\ \theta \end{bmatrix} = \begin{bmatrix} f^u \\ f^v \\ 0 \\ g^w \\ g^\theta \end{bmatrix}, \tag{6}$$

where the part $[C]$ represents the kinematic constraint, which should be satisfied on the interface between the fluid and the beam, and the parts $[D]$ and $[E]$ represent Eq. (5) for the beam. The kinematic constraint can be represented as follows:

$$u = 0,\ v = \dot{w} \quad \text{on the beam surface.} \tag{7}$$

Most previous studies on FSI problems have conventionally used the *explicit scheme*, where the procedure is as follows:

(i) compute the flow field with given boundary conditions on the given mesh;
(ii) compute the traction on the surface of the structure;
(iii) compute the deformation of the structure with the traction given in (ii);
(iv) update the meshes both for the fluid and the structure according to the deformation given in (iii);
(v) iterate (i)–(iv) until the convergence criteria for both the fluid and the beam are satisfied.

Although the above explicit scheme needs less computational time, it may not converge under certain circumstances (Hu et al., 1992, 2001). However, the present combined formulation does not have such a problem by virtue of its implicit nature and is stabler than the explicit scheme. When implementing the combined formulation with the ALE

technique, it is natural to use an *explicit–implicit scheme* (Hu et al., 1992, 2001). In the present study, we use a modified version of the explicit-implicit scheme, where the mesh nodes in the fluid domain are updated explicitly, while the deformation of the beam, the fluid flow field, and the mesh velocities are determined implicitly, as follows:

(i) solve the Laplace equation to obtain the mesh velocity with the boundary condition enforcing that it is equal to the velocity of the beam on the beam surface;
(ii) solve the total global matrix (Eq. (6)) for the flow field and the deformation of the beam with given boundary conditions;
(iii) iterate (i)–(ii) until the convergence criteria for both the fluid and the beam are satisfied;
(iv) update the meshes for both the fluid and the beam according to the mesh velocity and the deformation of the beam, respectively;
(v) go to (i).

More information on the combined formulation and the explicit-implicit scheme can be found in Hu (1996), Choi (2000), Choi and Joseph (2001), Hu et al. (2001), and Namkoong (2002).

Overall computation time is reduced significantly by AILU preconditioning [adapted incomplete LU (Nam et al., 2002)] of the global matrix. Further, the variable reordering and element reordering (Nam et al., 2002) are performed as bandwidth reduction methods to improve the performance of AILU preconditioning.

3. Nondimensional parameters

To determine the nondimensional parameters governing this fluid–structure system, the Navier–Stokes equation for the fluid and the Bernoulli–Euler beam equation for the structure are nondimensionalized by adopting the following definitions:

$$\mathbf{u}^* = \frac{\mathbf{u}}{U},\quad \mathbf{x}^* = \frac{\mathbf{x}}{L},\quad p^* = \frac{p}{\rho_f U^2},\quad t^* = \frac{t}{L^2\sqrt{\rho_s A/(EI)}},\quad w^* = \frac{w}{L}, \tag{8}$$

where U is the characteristic velocity and L the beam length. The resulting nondimensionalized equations are as follows:

$$\frac{1}{R_t}\frac{\partial \mathbf{u}^*}{\partial t^*} + (\mathbf{u}^*\cdot\nabla^*)\mathbf{u}^* = -\nabla^* p^* + \frac{1}{\mathrm{Re}}\nabla^{*2}\mathbf{u}^*, \tag{9}$$

$$\frac{\partial^2 w^*}{\partial t^{*2}} + \frac{\partial^4 w^*}{\partial x^{*4}} = R_f p^*. \tag{10}$$

In addition to the Reynolds number, Re ($=\rho_f UL/\mu$), two nondimensional parameters appear in the above equations, which are defined as follows: [1]

$$R_t = UL\sqrt{\frac{\rho_s A}{EI}} = \frac{L^2\sqrt{\rho_s A/(EI)}}{L/U} = \frac{\text{beam time scale}}{\text{convection time scale}}, \tag{11}$$

$$R_f = \frac{\rho_f U^2 b}{EI/L^3} = \frac{\text{fluid inertia force}}{\text{elastic restoring force}}, \tag{12}$$

$$R_t^2 = R_f\frac{h}{L}\frac{\rho_s}{\rho_f}. \tag{13}$$

The appearance of the nondimensional parameter R_t is due to the use of the beam time scale ($=L^2\sqrt{\rho_s A/(EI)}$) for nondimensionalizing the time as in Eq. (8), instead of the convection time scale ($=L/U$). When R_t is small, the convection time scale of the flow is larger than the beam time scale and the time derivative term in the nondimensionalized Navier–Stokes equation (Eq. (9)) becomes large. That is, the beam vibrates many times while the fluid particle moves by a characteristic length scale L due to convection.

The appearance of the nondimensional parameter R_f is due to the use of the fluid inertia force ($=\rho_f U^2$) for nondimensionalizing the fluid pressure as in Eq. (8), instead of the elastic restoring force of the beam ($=EI/(L^3 b)$). When R_f is large, the fluid inertia force is larger than the elastic restoring force of the beam and the beam deforms more.

[1] Cf. Païdoussis' (1998, 2003) dimensionless flow velocity.

As is seen in Eq. (13), R_t and R_f are not independent of each other. Once the ratio of the beam height to the beam length h/L and the density ratio ρ_s/ρ_f are determined, R_t is proportional to the square root of R_f. Eventually, the nondimensional parameters governing the fluid-structure system considered in the present study can be represented as follows:

$$\left(\mathrm{Re},\ R_t,\ \frac{h}{L},\ \frac{\rho_s}{\rho_f}\right) \quad \text{or} \quad \left(\mathrm{Re},\ R_f,\ \frac{h}{L},\ \frac{\rho_s}{\rho_f}\right). \tag{14}$$

4. Computational results

4.1. Static fluid–structure interaction in a steady flow

We first perform calculations of a steady two-dimensional laminar channel flow divided by a plate and compare the results with those of Wang (1999). By assuming that the deformation of the plate is small and the flows are fully developed, Wang (1999) derived equations for the pressure and shear stress on the upper and lower surfaces of the plate. From these equations, he derived an ordinary differential equation for the deformation of the plate and solved it by using a finite difference method, and compared the results with those obtained by using the general-purpose commercial code ADINA.

Thus, the geometry and parameter are the same as those of Wang (1999), i.e., $L = 0.75\,\mathrm{m}$, $h = 0.01\,\mathrm{m}$, $\rho_s = 7800\,\mathrm{kg/m^3}$, $E = 2.0 \times 10^{11}\,\mathrm{Pa}$, $\rho_f = 1000\,\mathrm{kg/m^3}$, $\mu = 0.00113\,\mathrm{kg/(m\,s)}$, $(h/L = 0.0133, \rho_s/\rho_f = 7.8)$. The following two cases are considered according to the shape of the channel (see Fig. 1 for geometry and notations):

(a) uniform channel: $\mathrm{Re}_1 = 177.0$, $\mathrm{Re}_2 = 354.0$, $U_{\mathrm{avg1}} = U_{\mathrm{avg2}} = 0.01\,\mathrm{m/s}$, $H_1(x) = 0.02\,\mathrm{m}$, $H_2(x) = 0.04\,\mathrm{m}$, $R_t = 5.13 \times 10^{-4}$, $R_f = 2.53 \times 10^{-6}$;

(b) convergent channel: $\mathrm{Re}_1 = 318.6$, $\mathrm{Re}_2 = 118.0$, $U_{\mathrm{avg1}}\big|_{x=0} = 0.012\,\mathrm{m/s}$, $U_{\mathrm{avg2}}\big|_{x=0} = 0.0033\,\mathrm{m/s}$, $H_1(x) = (0.03—x/75)\,\mathrm{m}$, $H_2(x) = (0.04–2\ x/75)\,\mathrm{m}$, $R_t = 3.59 \times 10^{-4}$, $R_f = 1.24 \times 10^{-6}$;

where we use the bulk velocity of the total channel flow as the characteristic velocity of the fluid, U, which is needed in calculating two nondimensional parameters R_t and R_f, and defined as follows:

$$U = \frac{U_{\mathrm{avg1}}\big|_{x=0} H_1(0) + U_{\mathrm{avg2}}\big|_{x=0} H_2(0)}{H_1(0) + H_2(0)}. \tag{15}$$

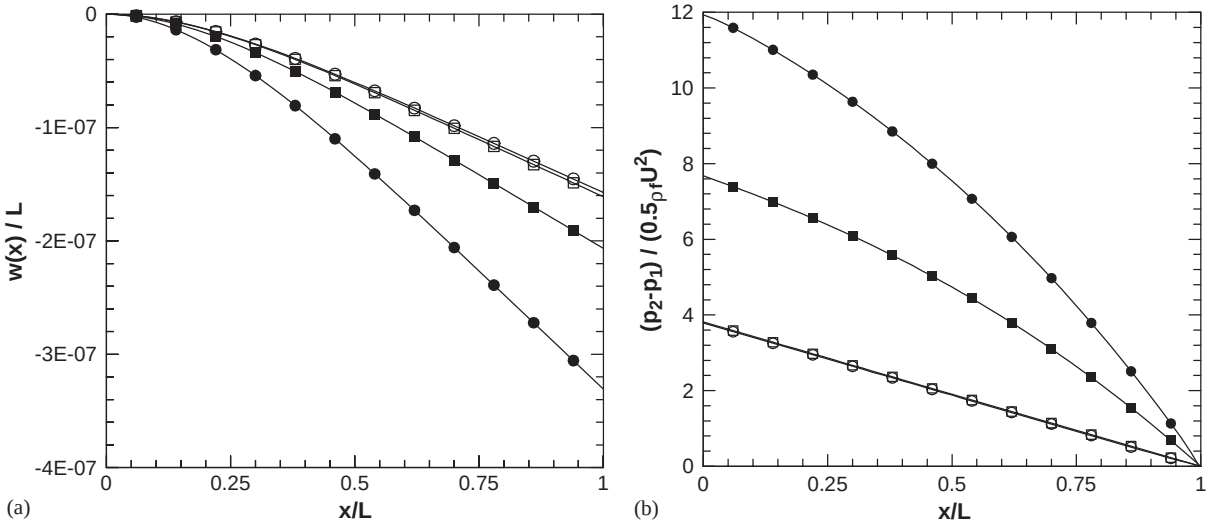

Fig. 3. Comparisons of (a) displacement and (b) pressure difference with analytic solutions by Wang (1999) for steady laminar channel flow: —○—, present result for the uniform channel; —□—, analytical solution by Wang (1999) for the uniform channel; —●—, present result for the convergent channel; —■—, analytical solution by Wang (1999) for the convergent channel.

The bounds of the computational domain in the streamwise direction are $x \in [0, 1.5\,\mathrm{m}]$ for the uniform channel and $x \in [0, 1.2\,\mathrm{m}]$ for the convergent channel. The inlet velocity profile is set to be parabolic to compare the results with the analytic results of Wang (1999), where fully developed laminar channel flows were assumed. The traction-free condition is set as the boundary condition at the channel exit. The beam is clamped at the left end and is free at the right end, as can be seen in Fig. 1.

The displacements and pressure differences between the upper and the lower surfaces of the beam for the two cases mentioned above are compared with the analytic solutions of Wang (1999) in Fig. 3. Note that w/L is very small, i.e. $\mathcal{O}(10^{-7})$, because both E and h are relatively large, while the displacement of a clamped-free beam due to a uniformly distributed load p_0 per unit length is $p_0L^4/(8EI)$, where $I = bh^3/12$. There exists a good agreement in the case of the uniform channel, but our results predict larger displacement and larger pressure difference in the case of the convergent channel. As is seen in Fig. 3(b), the pressure difference nondimensionalized by the dynamic pressure in the case of the convergent channel is 11.93, which is quite different from the value 7.68 of Wang (1999). It seems that this difference is due to the assumption of a fully developed flow when Wang derived the analytical solution, despite the fact that both the upper and the lower channels are convergent. To show this, the streamwise velocity profiles of both the upper and the lower channels at the exit are shown in Fig. 4(a), where the y coordinate is normal to the beam surface. The maximum velocities are calculated from the mass conservation when obtaining the parabolic profiles. One can see that the velocity profiles of the present study are not parabolic but inclined toward the beam surfaces, so that the shear stresses on both surfaces will be larger, which typically holds in the convergent channel. To be more specific, we recall that $\tau_w = -0.5h_c(\partial p/\partial x)$ for a fully developed laminar channel flow of height h_c. Then the larger shear stresses will in turn increase the pressure gradients along the channel, so that the pressure differences between the inlet and the exit of the channel will also increase ultimately.

The pressure gradients $(\partial p/\partial x)$ on the upper and the lower surfaces of the beam are compared with the analytical solutions of Wang (1999) in Fig. 4(b), where one can see that the pressure gradients in the present study increase rapidly, and the differences between the present results and those of Wang (1999) also increase rapidly as the free end of the beam is reached. As mentioned earlier, the bounds of the computational domain in the streamwise direction are set to be $x \in [0, 1.2\,\mathrm{m}]$, which corresponds to one and a half times the beam length ($L = 0.75\,\mathrm{m}$), for physically more reasonable results. A contour plot of the wall-normal velocity v around the free end of the beam is shown in Fig. 5, where one can see that it amounts to about 10% of the bulk velocity U around the free end and cannot be neglected. Wang (1999) did not consider the region beyond the free end of the beam and neglected the wall-normal velocity, and simply imposed the condition that the pressures in the upper and the lower channels at the exit ($x = 0.75\,\mathrm{m}$) should be equal. This is the main reason why the pressure gradients of the present result are different from those of the analytic solution of Wang (1999). If $\partial p/\partial x$ were calculated incorrectly, the pressure, which was obtained by integrating the

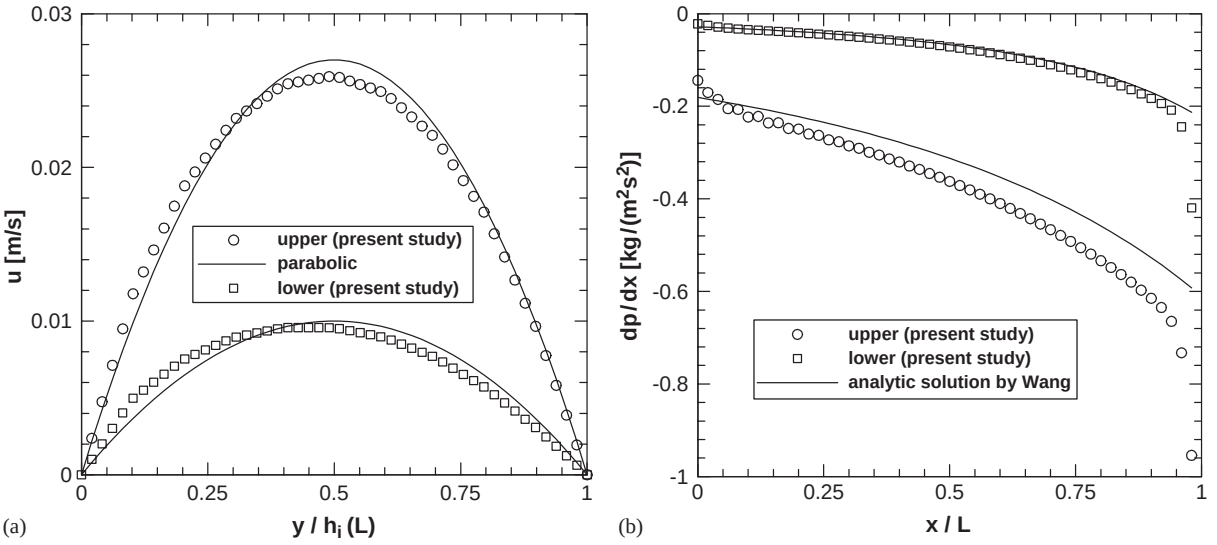

Fig. 4. Comparisons of (a) the streamwise velocity profiles at the exit and (b) the pressure gradients on the beam surfaces with the analytical solution by Wang (1999) for a steady laminar convergent channel flow.

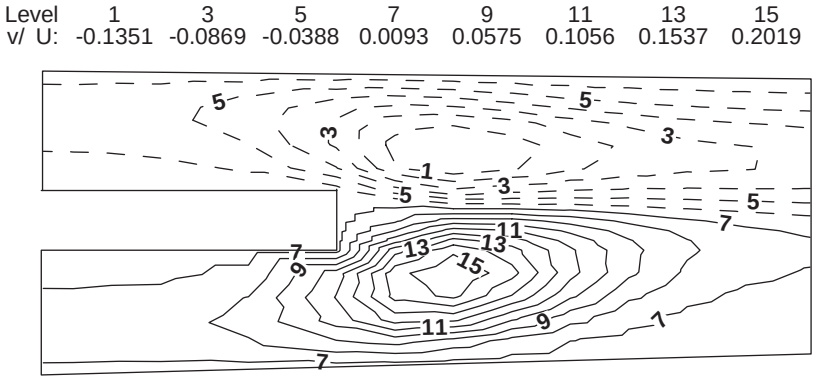

Fig. 5. Contour plot of the wall-normal velocity v around the free end of the beam.

pressure gradient in Wang (1999), would also be incorrect and the error might have increased due to integration. If the pressure is incorrect, the displacement due to the pressure difference on the beam surfaces could have errors, too.

Wang (1999) showed that the results from the commercial package ADINA agree well with those from the analytical solution. However, in laminar calculations with ADINA, constant pressure conditions were imposed both at the upper and the lower inlets instead of the velocity conditions, and the pressure difference at the inlets was set almost equal to that from the analytical solution (Wang, 2002). Taking all the above facts into account, one can conclude that the analytical approach of Wang (1999) may have errors in the case of the convergent channel, while it predicts the correct results in the case of the uniform channel.

4.2. Dynamic fluid–structure interaction in unsteady flow

Let us now consider the dynamic problem concerning the same convergent channel as in Section 4.1. The computational domain, Reynolds numbers, and the properties of the beam are the same as in Section 4.1, i.e., $L = 0.75\,\mathrm{m}$, $h = 0.01\,\mathrm{m}$, $\rho_s = 7800\,\mathrm{kg/m^3}$, $E = 2.0 \times 10^{11}$ Pa, $\mathrm{Re}_1 = 318.6$, $\mathrm{Re}_2 = 118.0$. Both the fluid and the beam are initially at rest and for $t > 0$ the parabolic velocity profiles are imposed at the inlets and traction-free conditions at the exits.

4.2.1. Dynamic FSI at the same parameters as in static FSI

To confirm that the code developed in the present study predicts correct results in dynamic FSI problems, we consider first the same fluid properties as in Section 4.1 [$\rho_f = 1000\,\mathrm{kg/m^3}$, $\mu = 0.00113\,\mathrm{kg/(m\,s)}$]. Since $R_t = 3.59 \times 10^{-4}$ in this case, the time scale of the beam is much less than the convection time scale of the fluid so that time increment should be very small. We set $\Delta t = 0.003\,\mathrm{s}$, considering the undamped period of oscillation of the first mode of a clamped-free beam, which is represented by

$$\tau = \frac{2\pi}{1.875^2} L^2 \sqrt{\frac{\rho_s A}{EI}}. \tag{16}$$

From Eq. (16), $\tau \approx 0.069\,\mathrm{s}$, and about 23 computations are performed per one oscillation period of the beam at the first undamped natural frequency. It is also noted that since $R_f = 1.24 \times 10^{-6}$ in this case, the elastic restoring force of the beam is much larger than the inertia force of the fluid. Thus, the displacement of the beam will be very small.

The time histories of the displacement at the free end of the beam are shown in Fig. 6, where one can easily see that the beam oscillates around the displaced position obtained from the static FSI computation in Section 4.1. From this, it seems that the present code also predicts correct results in dynamic FSI problems. The fact that the amplitude of oscillation is reduced with the passage of time regardless of the neglected internal damping of the beam is due to the damping by fluid viscosity. This damping effect depends on the dynamic viscosity μ and the density ρ_f of the fluid, which will be explained in detail in Section 4.2.2. The abscissa in Fig. 6 represents the time t nondimensionalized by τ. It is seen in Fig. 6(b) that the beam oscillates at the first undamped natural frequency during some initial periods, say, for $t/\tau < 4$ before the oscillation frequency is rapidly reduced. The Fourier spectrum of the data in Fig. 6(a) is shown in Fig. 7, where the abscissa represents the frequency f, also nondimensionalized by τ. Note that the dominant frequency is about $\frac{1}{10}$ times the first undamped natural frequency. This phenomenon results from the FSI and can be explained by the added mass concept, which will be dealt with in detail next.

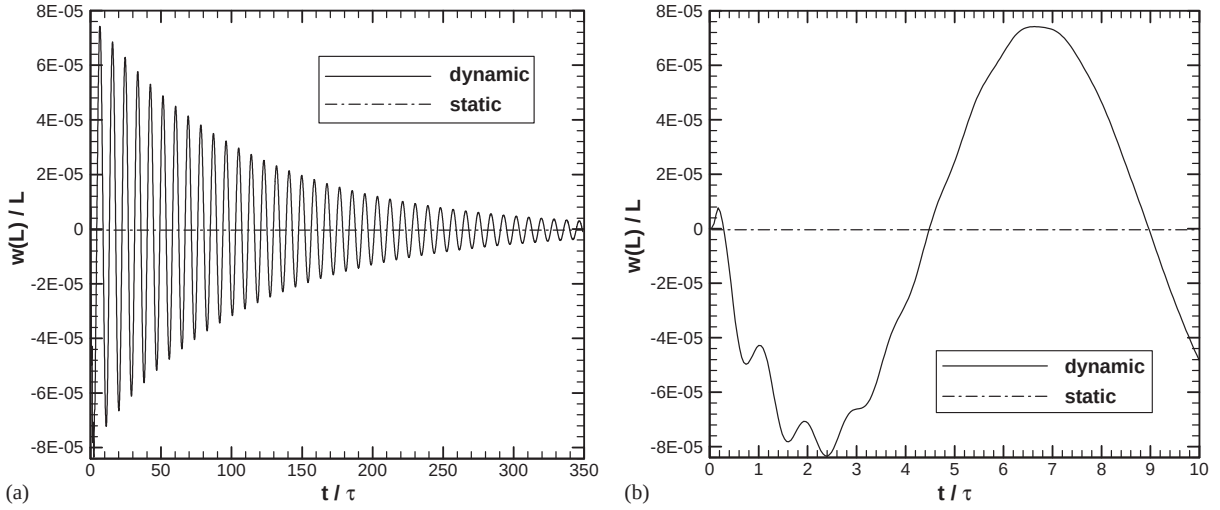

Fig. 6. (a) Long-term and (b) initial history of $w(L)$.

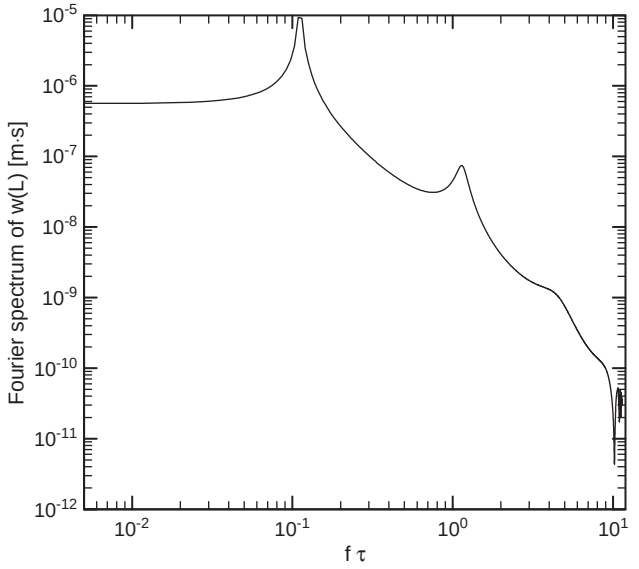

Fig. 7. Fourier spectrum of $w(L)$ in Fig. 6(a).

4.2.2. Damping by the fluid viscosity and the effect of the added mass

To investigate the damping by the fluid viscosity and the added mass, the following three sets of fluid properties are tested in the convergent channel with the Reynolds numbers fixed as in Section 4.2.1 ($\mathrm{Re}_1 = 318.6$, $\mathrm{Re}_2 = 118.0$):

Case 1: $\rho_f = 1.0\,\mathrm{kg/m^3}$, $\mu = 1.13 \times 10^{-4}\,\mathrm{kg/(m\,s)}$, $U_{\mathrm{avg1}}\big|_{x=0} = 1.2\,\mathrm{m/s}$, $U_{\mathrm{avg2}}\big|_{x=0} = 0.33\,\mathrm{m/s}$, $R_t = 1.29 \times 10^{-2}$, $R_f = 1.24 \times 10^{-5}$.

Case 2: $\rho_f = 1.0\,\mathrm{kg/m^3}$, $\mu = 1.13 \times 10^{-5}\,\mathrm{kg/(m\,s)}$, $U_{\mathrm{avg1}}\big|_{x=0} = 0.12\,\mathrm{m/s}$, $U_{\mathrm{avg2}}\big|_{x=0} = 0.033\,\mathrm{m/s}$, $R_t = 1.29 \times 10^{-3}$, $R_f = 1.24 \times 10^{-7}$.

Case 3: $\rho_f = 10.0\,\mathrm{kg/m^3}$, $\mu = 1.13 \times 10^{-4}\,\mathrm{kg/(m\,s)}$, $U_{\mathrm{avg1}}\big|_{x=0} = 0.12\,\mathrm{m/s}$, $U_{\mathrm{avg2}}\big|_{x=0} = 0.033\,\mathrm{m/s}$, $R_t = 1.29 \times 10^{-3}$, $R_f = 1.24 \times 10^{-6}$.

In Case 2, the density is the same as in Case 1 but the dynamic viscosity is $\frac{1}{10}$ of that in Case 1. On the other hand, in Case 3, the dynamic viscosity is the same as in Case 1 but the density is 10 times that in Case 1. The nondimensional parameters R_t and R_f are also given for each case, from which it is expected that the displacement and the amplitude will

be the largest in Case 1 because R_f is the largest. The time history of the displacement at the free end of the beam during $0<t/\tau<10$ is shown in Fig. 8. As is expected, the amplitudes of oscillation become larger in the order of Cases 2, 3, and 1.

It is very difficult to know from Fig. 8 in which case the damping by the viscosity is the largest. A measure of the damping can be represented by the logarithmic decrement δ, which is often used to calculate the damping ratio ζ in the free vibration of a simple mass-spring-damper system. The logarithmic decrement δ is defined and related to the damping ratio ζ as follows:

$$\delta = \ln\left(\frac{w_i - w_{\text{steady}}}{w_{i+1} - w_{\text{steady}}}\right) = \frac{2\pi\zeta}{1-\zeta^2}, \tag{17}$$

where w_i and w_{i+1} denote ith and $(i+1)$th local maximum values of the displacement, respectively, and w_{steady} is the steady state value of the displacement as $t \to \infty$. Although the vibration in the present study is not a free one, we use the logarithmic decrement as a measure of damping because the definition is simple and straightforward. The logarithmic decrement and the damping ratio calculated using Eq. (17) are shown in Fig. 9, where one can see that both the logarithmic decrement and the damping ratio become larger in the order of Cases 2, 1, and 3. Consequently, it is concluded that the larger the dynamic viscosity and the density of the fluid are, the larger the damping of the amplitude of beam oscillation is, when the Reynolds number and the geometry are fixed in a two-dimensional laminar channel divided by a plate.

Let us now turn our attention to the concept of added mass. When a body moves through a fluid, it must push a finite mass of the fluid out of the way. If the body is accelerated, the surrounding fluid must also be accelerated. The body behaves as if it were heavier by an amount called the *added mass* or *hydrodynamic mass* of the fluid (White, 2003), m_a. The added mass in a simple mass (m)–spring (k)–damper (c) system surrounded by a fluid can be represented as follows:

$$\begin{aligned} m\ddot{x} + c\dot{x} + kx &= -m_a\ddot{x}, \\ (m+m_a)\ddot{x} + c\dot{x} + kx &= 0. \end{aligned} \tag{18}$$

As is seen in Eq. (18), the original mass-spring-damper system is changed into a new system, where the mass is increased by m_a. The natural frequency of this new system becomes $\sqrt{k/(m+m_a)}$, which is smaller than $\sqrt{k/m}$. For a two-dimensional circular cylinder of radius a, the added mass is $\rho_f \pi a^2$, which is the mass of the fluid supposedly occupying the same area (or volume) as the cylinder, and is linearly proportional to the density of the fluid.

Therefore, when the beam under consideration is accelerated, the surrounding fluid as much as the added mass of the beam is also accelerated, so that the dominant frequency will be smaller than the first undamped natural frequency. The Fourier spectra of the displacement at the free end of the beam for the three test cases are shown in Fig. 10. Noting that

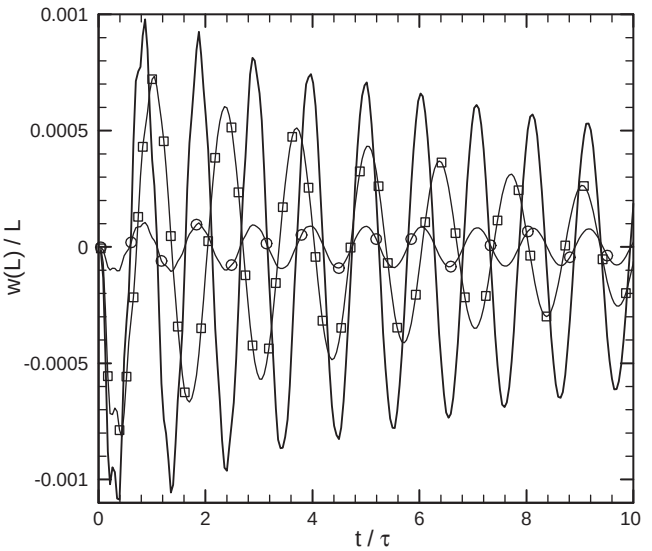

Fig. 8. Time history of $w(L)$ for the three test cases with different fluid properties but a fixed Reynolds number: ——, Case 1, $\rho_f = 1\,\text{kg/m}^3$, $\mu = 1.13\times10^{-4}\,\text{kg/(m s)}$; —○—, Case 2, $\rho_f = 1\,\text{kg/m}^3$, $\mu = 1.13\times10^{-5}\,\text{kg/(m s)}$; —□—, Case 3, $\rho_f = 10\,\text{kg/m}^3$, $\mu = 1.13\times10^{-4}\,\text{kg/(m s)}$.

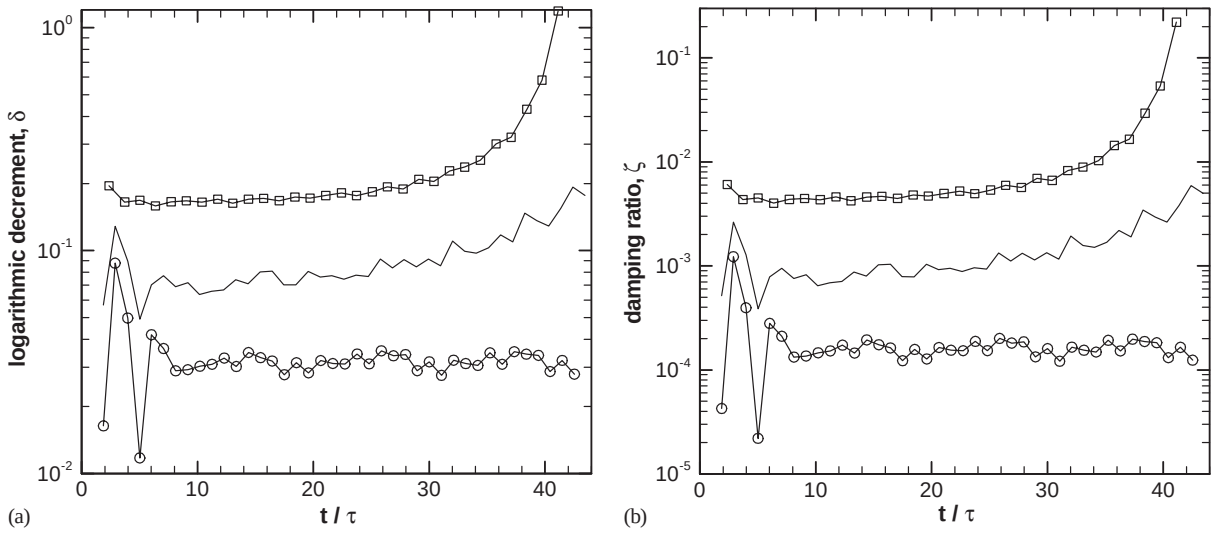

Fig. 9. (a) Logarithmic decrement δ and (b) damping ratio ζ, calculated using Eq. (17) for the three test cases with different fluid properties but a fixed Reynolds number: ——, Case 1, $\rho_f = 1\,\mathrm{kg/m^3}$, $\mu = 1.13 \times 10^{-4}\,\mathrm{kg/(m\,s)}$; —○—, Case 2, $\rho_f = 1\,\mathrm{kg/m^3}$, $\mu = 1.13 \times 10^{-5}\,\mathrm{kg/(m\,s)}$; —□—, Case 3, $\rho_f = 10\,\mathrm{kg/m^3}$, $\mu = 1.13 \times 10^{-4}\,\mathrm{kg/(m\,s)}$.

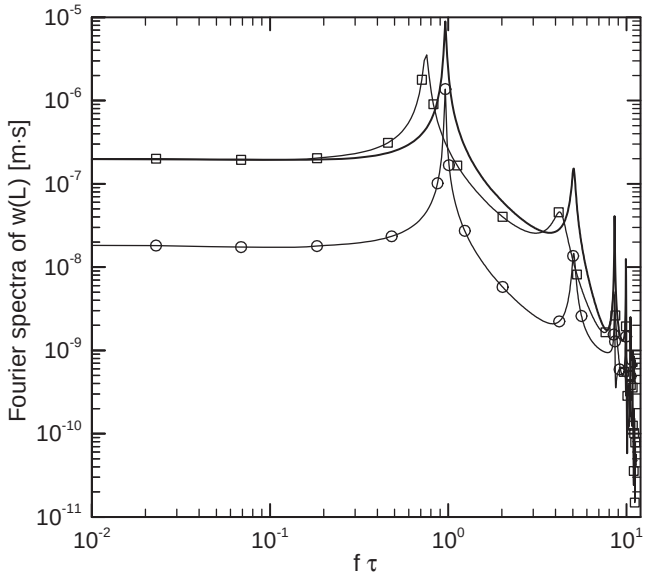

Fig. 10. Fourier spectra of $w(L)$ for the three test cases with different fluid properties but a fixed Reynolds number: ——, Case 1, $\rho_f = 1\,\mathrm{kg/m^3}$, $\mu = 1.13 \times 10^{-4}\,\mathrm{kg/(m\,s)}$; —○—, Case 2, $\rho_f = 1\,\mathrm{kg/m^3}$, $\mu = 1.13 \times 10^{-5}\,\mathrm{kg/(m\,s)}$; —□—, Case 3, $\rho_f = 10\,\mathrm{kg/m^3}$, $\mu = 1.13 \times 10^{-4}\,\mathrm{kg/(m\,s)}$.

the added mass is linearly proportional to the density of the fluid for a two-dimensional circular cylinder, one can guess that the added mass in Case 3 will be larger than those in Cases 1 and 2. It is easily seen from Fig. 10 that the dominant frequency in Case 3 is reduced while those in Cases 1 and 2 are not (note that $f\tau$ is the frequency nondimensionalized by the first undamped natural frequency and would be equal to 1 if the beam were not damped). In fact, $(f\tau)_1$ is 0.756 in Case 3 while it is 0.963 both in Cases 1 and 2. From this result, the cause of the reduction in the dominant frequency can be explained with the concept of the added mass.

For the case where the stiffness of the fluid is negligible, Blevins (1979) expressed the effect of added mass on the natural frequency of the plate as follows:

$$\frac{f_{\text{fluid}}}{f_{\text{air}}} = \frac{1}{\sqrt{1+(m_a/m)}}, \qquad \frac{m_a}{m} = \left(\frac{f_{\text{air}}}{f_{\text{fluid}}}\right)^2 - 1, \tag{19}$$

where f_{fluid} and f_{air} are the natural frequencies of the plate in the fluid and in the air, respectively, m is the mass of the plate, and m_a is the added mass of the plate. Eq. (19) will hold true only if the fluid does not modify the plate vibration mode shape. The magnitude of m_a is a function of several variables including the density and the viscosity of the fluid, the amplitude of vibration, the geometry of the plate, the plate's boundary conditions, its frequency mode number, and other factors (Païdoussis, 1998; Bartlett et al., 2001). Calculating the added mass using Eq. (19), one can get $m_a/m = 0.0789$ both in Cases 1 and 2, while $m_a/m = 0.748$ in Case 3. Note that the added mass calculated from Eq. (19) in Case 3 is almost 10 times as large as those in Cases 1 and 2. Using $(f\tau)_1 = 0.109$ in Fig. 7 (Section 4.2.1), one can get $m_a/m = 83.2$, which means that the added mass is 83 times as large as that of the beam itself. This large value of added mass is mainly due to the large density of the fluid. These results for the added mass are plotted in Fig. 11. It is easily seen in Fig. 11(b) that the added mass is linearly proportional to the density of the fluid but independent of the viscosity of the fluid for a clamped-free plate immersed in a two-dimensional laminar channel flow when the Reynolds number and the geometry are fixed.

4.3. Oscillation of a vertical plate in a cavity filled with a fluid

In order to demonstrate further the validity of the present code, the oscillation of a vertical plate in a cavity filled with a fluid is investigated in this section. A schematic describing the problem is shown in Fig. 12. Glück et al. (2001) investigated the same problem via a three-dimensional coupled simulation; the results in the present study will be compared with theirs, because in their study both the flow and the plate showed two-dimensional behavior, due to the symmetric boundary conditions in the z-direction. Note that the present simulation is two-dimensional, so that the plate can be modeled by a Bernoulli–Euler beam again. All other conditions of simulation are the same as those of Glück et al. (2001).

The length (L), the thickness (h), and the width (b) of the plate are 1.0, 0.06, and 0.4 m, respectively. The computational domain is taken as follows: the distance from the left wall of the cavity to the plate center plane is $10L$, the distance from the plate center plane to the right wall of the cavity is $40L$, and the height of the cavity is $6L$. A computational mesh at an instant is shown in Fig. 13, where a close-up view near the plate is also shown as an inset.

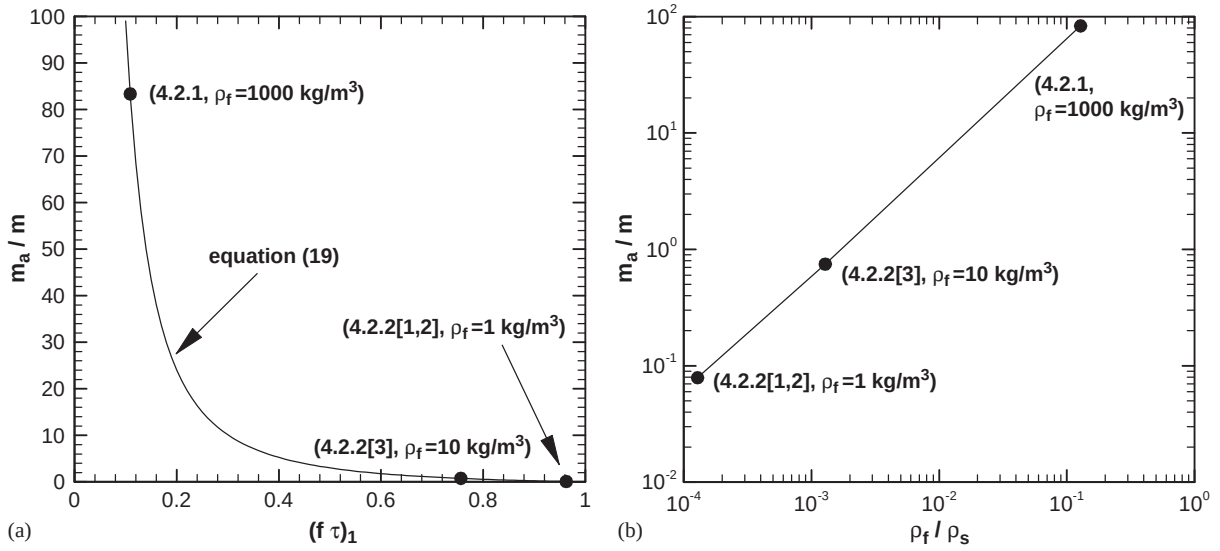

Fig. 11. (a) m_a/m versuss. $(f\tau)_1$ and (b) m_a/m versuss. ρ_f/ρ_s, calculated from Eq. (19).

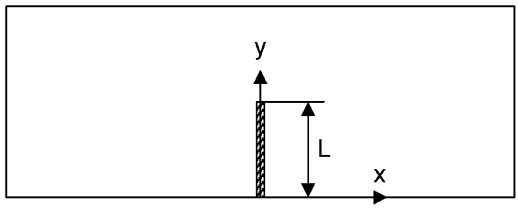

Fig. 12. A schematic describing the problem of oscillating vertical plate in a cavity filled with a fluid.

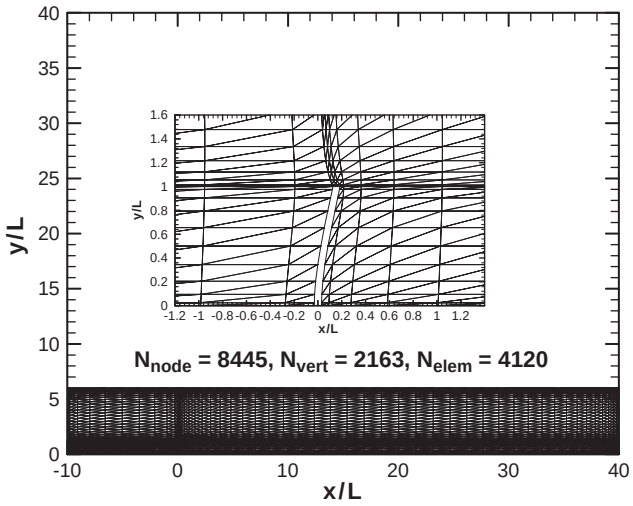

Fig. 13. A typical mesh for the problem of oscillating vertical plate in a cavity filled with a fluid: number of nodes = 8445, number of vertices = 2163, number of elements = 4120.

The following material properties are used: Young's modulus of elasticity $E = 2.5 \times 10^6$ Pa, density of plate material $\rho_s = 2550\,\mathrm{kg/m^3}$, density of the fluid $\rho_f = 1\,\mathrm{kg/m^3}$, and three different dynamic viscosities of the fluid $\mu = 0.2$, 1.0, and 5.0 kg/(m s), which result in laminar flows.

A time step (Δt) is chosen to be 0.1 s. From Eq. (17) in 4.2.2, $\tau \approx 3.30$ s, so that about 33 computations are performed per oscillation period of the first mode of the plate. During the first five steps, i.e., $t \leqslant 0.5$ s, a uniformly distributed load of 30 N/m is applied in order to excite the plate. From the sixth time step on, the beam is loaded by the reacting pressure resulting from the fluid flow.

Fig. 14 shows the horizontal displacement of the free end of the plate for three different viscosities of the fluid, where one can see that the higher the viscosity of the fluid is, the faster the plate is damped and reaches its initial state again. Because the densities of the fluid is all the same in the three cases, the damping of the amplitude of the plate oscillation will increase with the viscosity of the fluid, as explained in the previous subsection. That is, the larger the dynamic viscosity and the density of the fluid are, the larger the damping of the amplitude of beam oscillation is. This fact is confirmed again in Fig. 15, where the logarithmic decrement δ and the damping ratio ζ calculated by Eq. (17) are shown. In Fig. 16, the displacements of the free end of the beam for three different viscosities of the fluid are compared with those of Glück et al. (2001). There exist slight discrepancies in the frequency and the amplitude of oscillation but they decrease as the viscosity of the fluid increases. Considering that Glück et al. (2001) performed three-dimensional simulations by using a more complex plate model (not a beam model) with Poisson's ratio ($v_s = 0.35$) taken into account, these slight discrepances can be considered quite acceptable.

The fluid load in the x-direction for the case of $\mu = 0.2\,\mathrm{kg/(m\,s)}$ is compared with that of Glück et al. (2001) in Fig. 17, where there exist slight differences again in the frequency and the amplitude of oscillation. The fluid loads in the x-direction for three different viscosities of the fluid are also shown in Fig. 18, where one can see that the fluid load increases with the viscosity of the fluid.

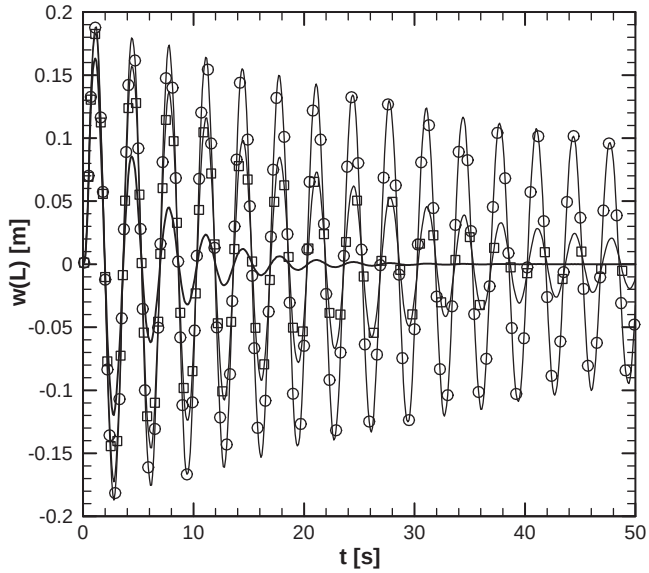

Fig. 14. Horizontal displacement of the free end of the plate for three different fluid viscosities: —○—, $\mu = 0.2\,\mathrm{kg/(m\,s)}$; —□—, $\mu = 1.0\,\mathrm{kg/(m\,s)}$; ——, $\mu = 5.0\,\mathrm{kg/(m\,s)}$.

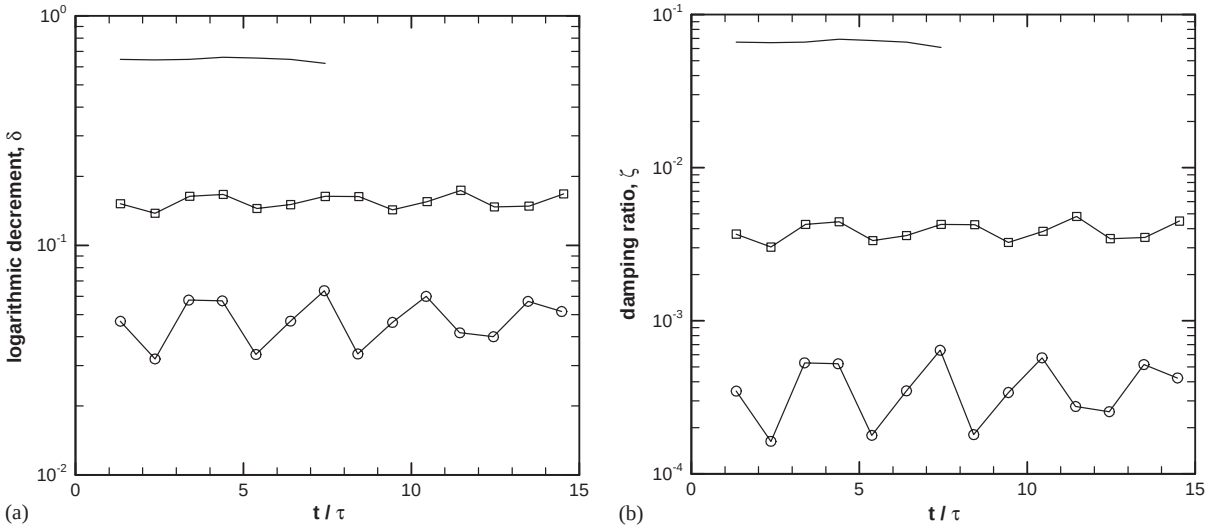

Fig. 15. (a) Logarithmic decrement δ and (b) damping ratio ζ calculated using Eq. (17) for three different fluid viscosities: —○—, $\mu = 0.2\,\mathrm{kg/(m\,s)}$; —□—, $\mu = 1.0\,\mathrm{kg/(m\,s)}$; ——, $\mu = 5.0\,\mathrm{kg/(m\,s)}$.

The Fourier spectra of the displacements and the fluid loads in the x-direction for three different viscosities of the fluid are shown in Figs. 19(a) and (b), respectively. The Fourier spectra of Glück et al. (2001) for the case of $\mu = 0.2\,\mathrm{kg/(m\,s)}$ are also shown for comparison. The first peak in the Fourier spectra of displacements for all three different viscosities of the fluid in the present study occurs at $(f\tau)_1 \approx 0.99$, while it occurs at $(f\tau)_1 \approx 1.03$ in the results of Glück et al. (2001). The difference is only about 4%, which may be negligible. The second peak in the Fourier spectra of the displacements for all three different viscosities of the fluid in the present study occurs at $(f\tau)_1 \approx 5.67$, while it occurs at $(f\tau)_1 \approx 5.53$ in the result of Glück et al. (2001). The difference is only about 2.5%, which may be negligible again. Note the difference in the order of magnitude between the Fourier coefficients at the first and the second peaks. That is, the

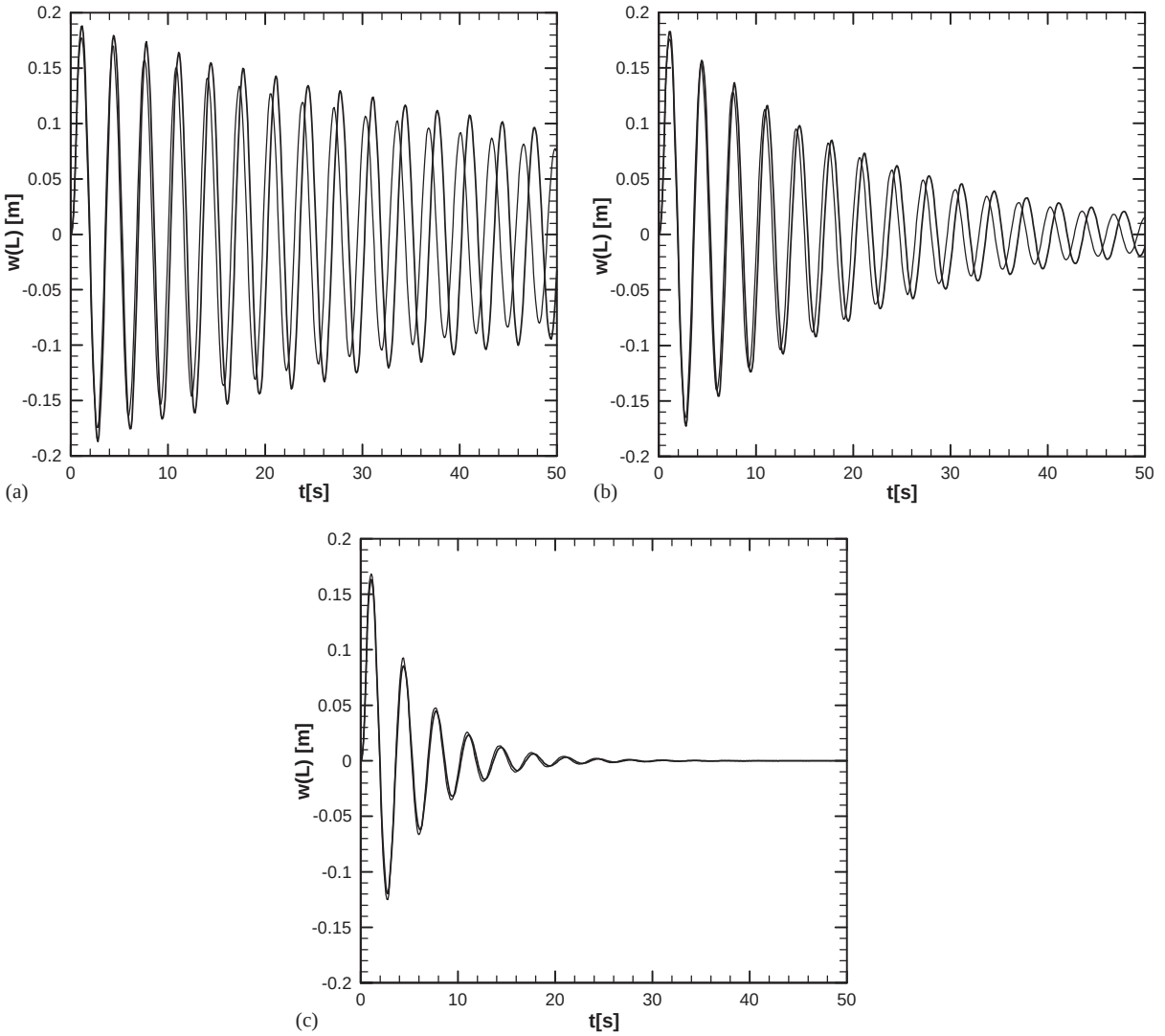

Fig. 16. Comparison of the displacements of the free end of the beam for three different fluid viscosities with previous results: (a) $\mu = 0.2\,\mathrm{kg/(m\,s)}$, (b) $\mu = 1.0\,\mathrm{kg/(m\,s)}$, and (c) $\mu = 5.0\,\mathrm{kg/(m\,s)}$; ————, Glück et al. (2001); ——, present study.

Fourier coefficient at the first peak is about 100 times larger than that at the second peak. This means that the displacement curve shows almost harmonic behavior, because the first eigenfrequency is dominant. One can reconfirm this in Figs. 14 and 16.

The first and the second peaks in the Fourier spectra of the fluid load in the x-direction occur at the same frequencies as those of the displacements. However, the Fourier coefficient of the fluid load in the x-direction at the first peak is only about 10 times larger than that at the second peak. This means that higher eigenmodes as well as the first eigenmode dominate the fluid load in the x-direction. Again, one can reconfirm this in Fig. 17. Glück et al. (2001) mentioned that "The same phenomena is described by Gasch and Knothe (1987), who compared the displacement and the moment of the clamped support of a beam performing bending oscillations."

Because the density of the fluid is very small compared to that of the beam, i.e., $\rho_f/\rho_s = 1/2550 \approx 0.0004$, the added mass is very small and negligible. Therefore, the frequency where the first peak in the Fourier spectra occurs is almost equal to the first undamped natural frequency (f_{n1}), i.e., $(f\tau)_1 = f/f_{n1} \approx 0.99$.

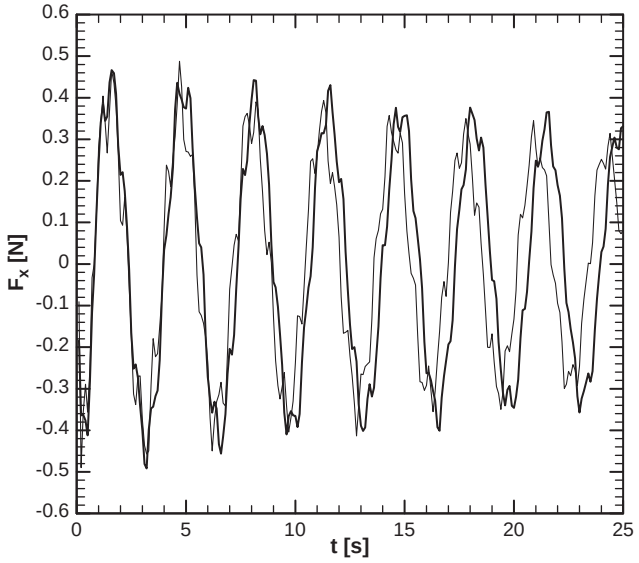

Fig. 17. Comparison of the fluid load in the x-direction for the case of $\mu = 0.2\,\mathrm{kg/(m\,s)}$ with a previous result: ————, Glück et al. (2001); ——, present study.

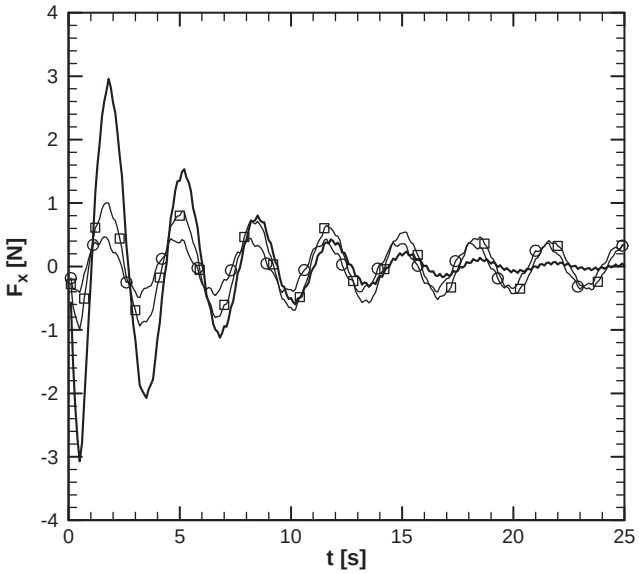

Fig. 18. Comparison of the fluid load in the x-direction for three different fluid viscosities: —○—, $\mu = 0.2\,\mathrm{kg/(m\,s)}$; —□—, $\mu = 1.0\,\mathrm{kg/(m\,s)}$; ——, $\mu = 5.0\,\mathrm{kg/(m\,s)}$.

5. Conclusions

Two dynamic FSI problems where the structure can be simply modeled by a Bernoulli–Euler beam were investigated: a two-dimensional laminar divided-channel flow and oscillation of a vertical plate in a cavity filled with a fluid. A P2P1 Galerkin FEM was used for the Navier–Stokes equation with the ALE technique and a Galerkin FEM for the equation of motion for the beam, so that these two equations were consolidated and solved using the combined formulation and a modified explicit–implicit scheme.

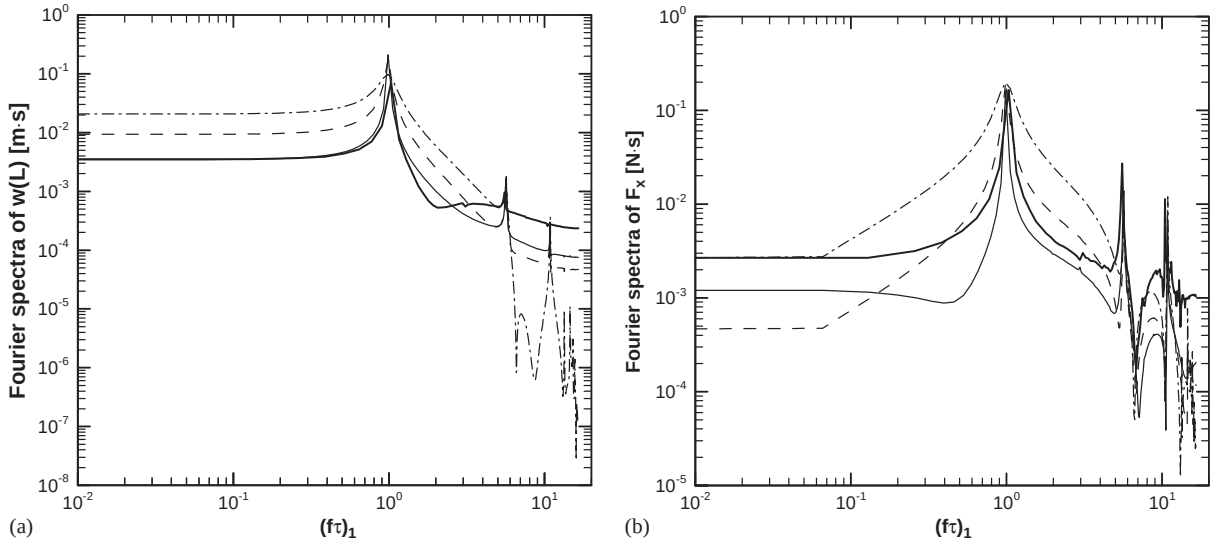

Fig. 19. Fourier spectra of (a) the displacements and (b) the fluid load in the x-direction: ——, $\mu = 0.2\,\mathrm{kg/(m \cdot s)}$, Glück et al. (2001); ————, $\mu = 0.2\,\mathrm{kg/(m\,s)}$, present study; - - - - - - , $\mu = 1.0\,\mathrm{kg/(m\,s)}$, present study; – – – – – –, $\mu = 5.0\,\mathrm{kg/(m\,s)}$, present study.

To validate the method developed in the present study, the static FSI problems, which are the same as in Wang (1999), were examined and compared. It was shown that the present results are in good agreement with those of the analytic solutions of Wang (1999) in the case of the uniform channel, but there are some discrepancies in the case of the convergent channel. A clear elucidation was given for these discrepancies by considering the velocity profiles of the two studies.

In addition to the Reynolds number, two nondimensional parameters, which govern this fluid–structure system, were proposed by nondimensionalizing the governing equations.

Investigation of the dynamic FSI in a two-dimensional laminar divided-channel flow demonstrated that for fixed Reynolds number and geometry the damping of the amplitude of plate oscillation increases as the dynamic viscosity and density of the fluid increase. It is also noteworthy that the added mass is linearly proportional to the fluid density but independent of the fluid viscosity so that the dominant frequency of the plate is reduced as the fluid density increases.

The dynamic FSI of a vertical plate in a cavity filled with a fluid was also investigated. The results were in good agreement with those from the three-dimensional coupled simulation of Glück et al. (2001). The added mass effect is negligible in this case, due to the very small density of the fluid compared to the density of the plate. The displacement curves show almost harmonic behavior, because the first eigenfrequency dominates, while the fluid load is also influenced by higher eigenmodes.

Acknowledgements

This work is supported by BK21 Project, Ministry of Education and Human Resources Development, and by Micro Thermal System Research Center, Korea Science and Engineering Foundation, Republic of Korea.

References

Bartlett, S., Winton, M., Clausen, P.D., 2001. An added mass theory for the base plate in a partially filled rectangular tank for use with FEA. Journal of Sound and Vibration 246, 211–223.

Blevins, R.D., 1979. Formulas for Natural Frequency and Mode Shape. Krieger, Malabar, FL, USA.

Choi, H.G., 2000. Splitting method for the combined formulation of the fluid–particle problem. Computer Methods in Applied Mechanics and Engineering 190, 1367–1378.

Choi, H.G., Joseph, D.D., 2001. Fluidization by lift of 300 circular particles in plane Poiseuille flow by direct numerical simulation. Journal of Fluid Mechanics 438, 101–128.

Dowell, E.H., Hall, K.C., 2001. Modeling of fluid–structure interaction. Annual Review of Fluid Mechanics 33, 445–490.

Ergin, A., Uğurlu, B., 2003. Linear vibration analysis of cantilever plates partially submerged in fluid. Journal of Fluids and Structures 17, 927–939.

Frandsen, J.B., 1999. Computational fluid–structure interaction applied to long-span bridge design. Ph.D. Thesis, Department of Engineering, Cambridge University, UK.

Gasch, R., Knothe, K., 1987. Strukturdynamik. Band 2: Kontinua und ihre Diskretisierung. Springer, London, UK.

Glück, M., Breuer, M., Durst, F., Halfmann, A., Rank, E., 2001. Computation of fluid–structure interaction on lightweight structures. Journal of Wind Engineering and Industrial Aerodynamics 89, 1351–1368.

Glück, M., Breuer, M., Durst, F., Halfmann, A., Rank, E., 2003. Computation of wind-induced vibrations of flexible shells and membrane structures. Journal of Fluids and Structures 17, 739–765.

Hesla, T. I., 1991. Combined formulation of fluid–particle problem. unpublished note.

Hu, H.H., 1996. Direct simulation of flows of solid–liquid mixtures. International Journal of Multiphase Flow 22, 335–352.

Hu, H.H., Joseph, D.D., Crochet, M.J., 1992. Direct simulation of fluid particle motions. Theoretical and Computational Fluid Dynamics 3, 285–306.

Hu, H.H., Patankar, N.A., Zhu, M.Y., 2001. Direct numerical simulations of fluid–solid systems using the arbitrary Lagrangian–Eulerian technique. Journal of Computational Physics 169, 427–462.

Kovacs, I., 1994. Synthetic wind for investigation in time-domain. ASCE Structures Congress, Atlanta, GA, USA.

Lam, K.Y., Wang, Q.X., Zong, Z., 2002. A nonlinear fluid–structure interaction analysis of a near-bed submarine pipeline in a current. Journal of Fluids and Structures 16, 1177–1191.

Nam, Y.S., Choi, H.G., Yoo, J.Y., 2002. AILU preconditioning for the finite element formulation of the incompressible Navier–Stokes equations. Computer Methods in Applied Mechanics and Engineering 191, 4323–4339.

Namkoong, K., 2002. Numerical analyses of dynamic fluid–structure interaction about a freely falling cylinder and a Bernoulli–Euler beam. Ph.D. Dissertation, School of Mechanical and Aerospace Engineering. Seoul National University, Seoul, Korea.

Païdoussis, M.P., 1998. Fluid–Structure Interactions: Slender Structures and Axial Flow, vol. 1. Academic Press, London, UK.

Païdoussis, M.P., 2003. Fluid–Structure Interactions, Slender Structures and Axial Flow, vol. 2. Elsevier Academic Press, London, UK.

Slone, A.K., Pericleous, K., Bailey, C., Cross, M., 2002. Dynamic fluid–structure interaction using finite volume unstructured mesh procedures. Computers and Structures 80, 371–390.

Wang, X., 1999. Analytical and computational approaches for some fluid–structure interaction analyses. Computers and Structures 72, 423–433.

Wang, X., 2002. Private communications.

White, F.M., 2003. Fluid Mechanics, fifth ed. McGraw-Hill, New York, USA.

Zahlten, W., 1998. Zur numerischen Simulation winderregter Strukturen. Habilitationsschrift, Fakultät für Bauingenieur- und Vermessungswesen. RWTH, Aachen, Germany.

Zhang, H., Zhang, X., Ji, S., Guo, Y., Ledezma, G., Elabbasi, N., deCougny, H., 2003. Recent development of fluid–structure interaction capabilities in the ADINA system. Computers and Structures 81, 1071–1085.